AN UNSTEADY FSI INVESTIGATION INTO THE CAUSE OF THE DISMASTING OF THE VOLVO 70 GROUPAMA 4

W. Menotti, Menotti Marine, France, wenceslas@menotti-marine.com
M. Durand, D. Gross and **Y. Roux,** K-Epsilon, France, mathieu@k-epsilon.com, david@k-epsilon.com, yann@k-epsilon.com
D. Glehen, GSea Design, France, denis@gseadesign.com
L. Dorez, Groupama Sailing Team, France, loic@groupamasailingteam.com

This paper describes the use of an unsteady fluid-structure interaction (FSI) tool as an investigative tool into the cause of the dismasting of the VOR 70 Groupama 4. As more than one rig component failed during the dismasting, the cause of failure was not immediately apparent. The investigation therefore required isolating the cause of failure between two closely related rig components. The FSI coupling process and the determination of the initial rig loading based on a steady FSI computation and measured data will be described. The setup for two unsteady failure cases will be discussed and the results of those investigations will be examined.

NOMENCLATURE

$[D]$	Damping matrix $\frac{\partial R}{\partial \dot{u}}$ (N.s.m^{-1})
$[K]$	Stiffness matrix $\frac{\partial R}{\partial u}$ (N.m^{-1})
$[M]$	Mass matrix $\frac{\partial R}{\partial \ddot{u}}$ (kg)
R	Residual force (N)
u	Position (m)
$\dot{u}$	Velocity (m.s^{-1})
$\ddot{u}$	Acceleration (m.s^{-2})
$\vec{U}_\infty$	Incident flow velocity (m.s^{-1})
$\vec{U}_\varphi$	Doublet induced velocity (m.s^{-1})
$\vec{U}_\omega$	Wake induced velocity (m.s^{-1})
$\vec{X}_i$	Vortex particle position (m)
$\vec{\Omega}_i$	Vortex particle vorticity (s^{-1})

1 INTRODUCTION

The 2011-2012 edition of the Volvo Ocean Race was notable for the number of rig failures that occurred during the course of the race. The cause of the dismasting of Groupama 4 on the leg between Auckland and Itajai in calm seas and moderate breeze was not immediately apparent based on examination of the recovered pieces, as more than one secondary structural member had failed during the dismasting. In particular, it was necessary to determine if the mast failure was due to the port side D1 or the port side first spreader failing. The determination of the cause of the failure therefore necessitated that an investigative structural analysis be performed. To perform such an analysis would require that a detailed structural model of the rig and sails be utilized in conjunction with an accurate description of the static and aerodynamic structural loads. ARAVANTI, the tool utilized, is composed of ARA, an unsteady, finite element structural solver capable of being tightly coupled to AVANTI, an unsteady potential flow solver or ISIS-CFD, an unsteady RANS solver [1, 2]. In the present study, the need for a rapid determination of the cause of failure and the sailing angle at the time of failure justified the use of the unsteady potential solver for the determination of aerodynamic loads. The structural model of the rig utilized was developed as part of a prior study, and hence could rapidly be brought to bear on the problem. While failure analysis is most often performed utilizing normal finite element structural software, this approach has a number of drawbacks. Specifically, the aerodynamic loads at the time of failure must either be estimated by the structural engineer or determined from an aerodynamic solver separately and then inputted into the structural solver. Furthermore, as the sail shape will change during the course of the failure; a significant drawback of this approach is that it is unable to account for changes in the aerodynamic loads over the course of the rig failure.

2 FLUID SOLVER

The flow code utilized in the present study, AVANTI is based on the assumptions that underpin potential flow; namely that the flow is incompressible, irrotational, and inviscid. The code combines a constant-strength, doublet surface representation of the bodies with a vortex particle method for the wake [3, 4]. The flow problem is thus broken down into two components:

- A lifting body problem based on a boundary integral;
- A wake problem in which vortex carrying particles in a Lagrangian framework are advected downstream in the wake.

Hence, AVANTI represents the flow field as the sum of the contribution of three components:

1) $\vec{U}_\infty$, the incident flow velocity;

2) $\vec{U}_\varphi$, the contribution induced due to the surface doublets;

3) $\vec{U}_\omega$, the contribution due to the vortex particles.

The vorticity of the individual particles must satisfy the Helmholtz equation. The equations for a particle i in the Lagrangian coordinate system, with the position of the

particle given as X_i and the particle vorticity given by Ω_i, are therefore:

$$\frac{d\vec{X}_i}{dt} = \frac{1}{4\pi}\sum_{j\neq i}\frac{\vec{\Omega}_j \times (\vec{X}_j - \vec{X}_i)}{\left|\vec{X}_j - \vec{X}_i\right|^3} + \vec{U}_\varphi(\vec{X}_j) + \vec{U}_\infty$$

$$\frac{d\vec{\Omega}_i}{dt} = \frac{3}{4\pi}\sum_{j\neq i}\frac{\vec{X}_j - \vec{X}_i}{\left|\vec{X}_j - \vec{X}_i\right|^5}\left(\vec{\Omega}_i \cdot \left(\vec{\Omega}_j \times (\vec{X}_j - \vec{X}_i)\right)\right)$$
$$+ \frac{\vec{\Omega}_j \times \vec{\Omega}_i}{\left|\vec{X}_j - \vec{X}_i\right|^3} + (\vec{\Omega}_i \cdot \nabla)(\vec{U}_\infty + \vec{U}_\varphi)(\vec{X}_i)$$

The principle advantage of using a vortex particle method over a panel wake method is the avoidance of wake panels intersecting one another during unsteady computations.

3 STRUCTURAL SOLVER

The unsteady finite element structural solver ARA, was developed by K-Epsilon as part of the project VOILE-NAV specifically with the aim of simulating the dynamic behaviour of sailboat rig [2, 5, 6]. To capture the unsteady behaviour in a time accurate manner, a Newmark-Bossak second-order accurate time scheme is used. The scheme is utilized because it provides the necessary filtering of non-physical high frequencies while maintaining an accurate description of the low frequencies. The scheme is conservative and hence avoids the generation of numerical energy in the case of very large nonlinearities. At each time step an equilibrium between the internal and external forces on all of the elements is required. To achieve this, the derivative of the forces with respect to the position, velocity, and acceleration of each element's nodes is found. The derivatives are then assembled into a mass matrix [M], damping matrix [D] and stiffness matrix [K]. The assembled matrix system of the form below is then solved utilizing the Newton-Raphson method after further rearrangement to be in a form suitable for the Newmark-Bossak scheme.

$$R = [M]\ddot{u} + [D]\dot{u} + [K]u$$

The rig and sails can be represented by membrane, shell, beam and cable elements. Sliding and contact elements are also implemented utilizing a penalization method. In the present study, membrane elements were utilized for the sails with beam elements for the mast, boom and spreaders. The beam elements utilized are shear-deformable Timoshenko beam elements. The membrane elements utilized are constant strain triangle (CST) elements suitable for large deformations. The stiffness matrix for the CST elements is found from the summation of the local stiffness properties of each ply used to fabricate the sail at that location. The local stiffness of each ply is determined from the density, orientation and stiffness of the fibres utilized in that region. The stiffness matrix of each element is thus able to account for the anisotropic material properties of competitive sail manufacturing techniques such as 3DI©, 3DL©, and D4© as well as local reinforcement patches.

4 FLUID-STRUCTURE COUPLING

Sails, are light structures where the entrained added mass of the air is of comparable or greater size to the mass of the sails themselves. This poses a particularly difficult case for unsteady FSI coupling schemes. The strong coupling between the fluid and structure requires that the coupling scheme has a tight coupling between the structure and fluid solvers. The coupling scheme utilized is a quasi-monolithic approach. It is based on an implicit, partitioned solver approach, but maintains the convergence and stability of a fully monolithic approach. This is achieved by utilizing an additional interface element in the structural solver derived from the Jacobian matrix of the interface. In the case of an exact Jacobian matrix, the coupling matrix is identical to that of a monolithic approach. In the present approach, a simplified Jacobian is computed. The Jacobian matrix allows the elimination of the use of under-relaxation, yielding a significant reduction in the number of coupling iterations required. The coupling process is outlined in figure 1 below. At each time step an FSI loop is started by first updating the wake particle positions and then computing the Jacobian matrix. A structural computation is then performed to convergence and the motions are transferred to the fluid solver. This is then followed by a fluid computation, after which convergence of the coupling is checked. If convergence has not been achieved the fluid forces are transferred back across the interface and the structural computation is repeated. Hence, fluid-structure convergence is achieved at each time step.
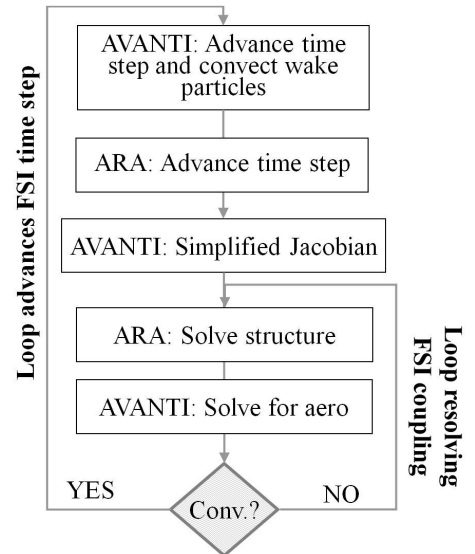

Figure 1: ARAVANTI unsteady FSI loop

5 STEADY CASE SETUP AND RESULTS

In order to perform the FSI computation, an accurate description of both the rig and the loads is required. As mentioned before, the structural properties and geometry of the rig and sails were developed before the current study as part of an earlier study. To replicate the structural loading at the time of failure, both the static and aerodynamic structural loads needed to be imposed. The static structural loads consisted primarily of the tensions applied to the shrouds. The initial tensions applied were taken from the measured dock tune tensions.

The aerodynamic loading was generated by a steady FSI computation based on the measured yacht and wind conditions at the time of the failure. These conditions are given in table 1.

Boat speed	12 knots
True wind speed	21 knots
Heel angle	22°
Heading	Close reach

Table 1: Sailing conditions

In order to obtain the correct aerodynamic loads, three criteria had to be met:
1) The sails had to be trimmed to a realistic setting for the given wind conditions and boat speed.
2) The forestay had to have a tension of 10 tons.
3) The heeling moment generated had to match the righting moment.

To achieve these aims, the jib was first trimmed optimally. The main sail was then used to achieve the correct heeling moment. The resulting steady loads are given in table 2.

Rig component	Line/Port side tension (kN)	Starboard side tension (kN)
V1	137.3	65.2
V2	107.1	63.5
V3	94.4	63.6
D1	49.4	10.0
D2	31.3	1.8
D3	13.1	0
D4	94.6	64.0
Runner	-	87.3
Forestay	105.0	-
Main halyard	31.0	-
Main sheet	29.2	-
Jib halyard	47.4	-
Jib sheet	21.5	-

Table 2: Steady shroud, sheet and halyard tensions

6 UNSTEADY SETUP AND RESULTS

The resulting sail flying shape and deformed shape of the rig from the steady computation was utilized for the initial shape and stresses of the unsteady computations. In order to model the sudden failure of a rig component, the member was made to no longer carry structural loads. This was accomplished for the D1 by changing the cable length to be very large such that it could no longer be under tension. The spreader failure was modelled by changing the element stiffness to 0, such that it no longer resisted applied loads. Failure of structural members was assessed based on the stress exceeding the ultimate strength of the member. As ARAVANTI does not have a built in capability to represent the effect of the failure of a structural element, if an element was determined to have failed, the computation was repeated with that element having its failure imposed at the time it exceeded its ultimate strength. The resulting time histories of the mast bending moments and deflections were then utilized to determine the mast failure point.

Three unsteady computations were performed as part of the study :
1. A computation where the port side D1 is made to fail.
2. A computation where the port side first spreader is made to fail.
3. A computation where the port side first spreader is made to fail and after which the port side D1 is made to fail 0.116 s later.

The third computation was performed based on feedback from the structural engineer, who indicated a failure should occur then. For the present paper, the results of the first and third computations will be presented. It should be noted that the D1 case also leads to the eventual failure of the first spreader. However, a D1 computation with an imposed failure of the spreader was not performed as the conclusion as to the cause of failure had already been drawn and such a computation would have required a slight modification to the way ARAVANTI stores beam stiffness properties to accommodate such a case. For reasons of confidentiality, the correct failure case cannot be identified, but a number of results related to the two failure cases can be given. Both cases are given with the initial failure occurring at t= 0 s.

6.1 SHROUD TENSIONS

The time histories of the tensions in the shrouds following the failure of the D1 are shown in figure 2. The loss of tension in the port D1 is visible at t= 0 s. The tensions undergo a rapid change immediately following the prescribed failure of the port D1, with an increase in tension on the starboard side and decrease in tension on the port side. The tensions then begin to gradually increase for the port side V1 and D2 while decreasing for all of the starboard side elements as the mast and spreaders continue to deflect. The port D3 and starboard D1 are rapidly unloaded until slack, with the starboard D2 following soon thereafter.
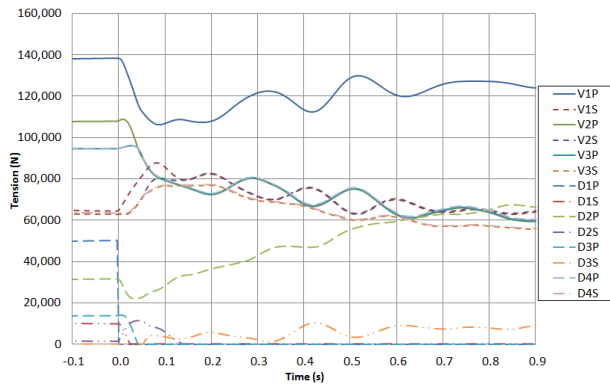
Figure 2: Time history of the shroud tensions, D1 case

Similarly, the tensions for the spreader failure case in figure 3 exhibit an initial increase in tension on the starboard side and decrease in tension on the port side. However, unlike the D1 failure case, the port D2 initially becomes completely slack before the tension begins to increase again as the rig continues to deflect. The starboard D1 initially sees a rise in tension, but then slackens with further rig deflection. The port D3 remains under tension. The imposed failure of the port D1 is visible at 0.116 s.
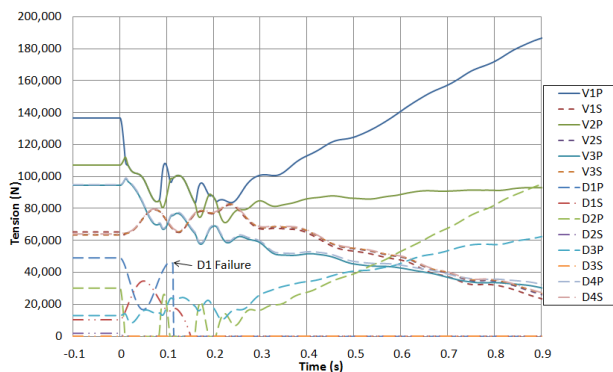
Figure 3: Time history of the shroud tensions, spreader case

6.2 SPREADER DEFLECTION

Unlike the shroud tensions, there is no inflection in the time history of the spreader maximum vertical bending curvature, as shown for the D1 case in figure 4. The deflections increase gradually with time. Significant deflections occur for the first spreader and to a lesser extent the second spreader.

In comparison to the D1 case, the spreader failure case curvature in figure 5 shows a much greater deflection of the second spreader.
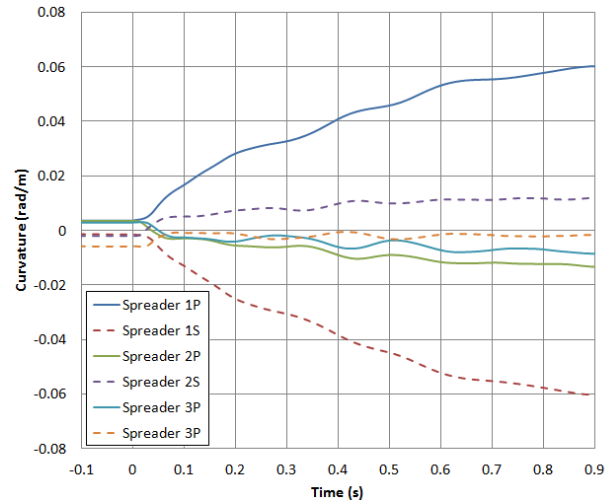

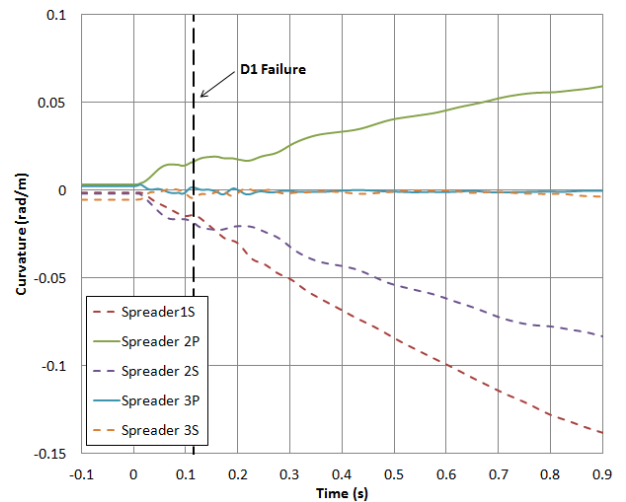Figure 4: Maximum spreader vertical bending curvature, D1 case

Figure 5: Maximum spreader vertical bending curvature, spreader case

6.3 MAST BENDING MOMENT AND DEFLECTION

The ability for a failure case to cause a failure of the other suspected rig element was an important consideration in the assessment of the failure mode. However, the mast failure location also needed to be correctly located. As mentioned before, ARAVANTI does not have a built in capability to represent component failure. Therefore, determining when the mast first reaches its ultimate strength was necessary to determine where failure occurred. The time histories of the transverse bending moment for both failure cases are presented in figure 6. The bending moment is initially small from 0 to 0.1 seconds. The bending moment then begins to steadily increase both in magnitude and extent along the mast length. The bending moment is concentrated in the lower portion of the mast; there is very little deflection in the upper portion of the mast. The bending moments are concentrated in two regions along the mast for both cases. The location of the two large bending moment regions is located further up the mast for the spreader case. The regions with large

bending moments are also more extensive and are of greater magnitude for the spreader case compared to the D1 case. The location along the mast of the largest bending moments does not change significantly over time. The growth rate of the bending moment is indicative of the rate by which the mast is deforming. The two cases exhibit noticeable differences in the growth of the bending moment. In particular, the lower region of the mast for the D1 case begins to have a bending moment greater than 50,000 N.m by 0.14 s, while the upper large bending moment region does not reach a comparable level until 0.34 s. In contrast, the two large bending moment regions of the spreader case achieve such a bending moment nearly simultaneously at 0.31 s. The curvature and bending deflection dynamic behaviours are therefore markedly different between the two cases. The difference in the deformation behaviour is visible in the time lapse images of the rig undergoing failure in figures 7 and 8. The lower region of curvature is more pronounced for the D1 case at 0.125 s. By 0.25 s the deflections of the spreader case have become larger relative to the D1 case. The difference in the location of the deflections is clearly visible. For the D1 case the upper high curvature region is located close to the first spreader with the lower high curvature region much closer to the foot of the mast. In contrast, for the spreader case the lower region of high curvature is located close to the first spreader with the upper region located closer to the second spreader.
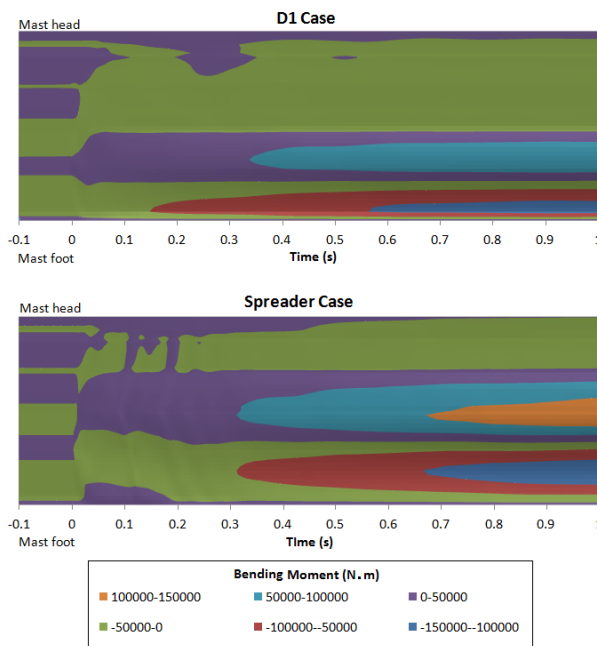

Figure 6: Time history of mast bending moments

7 CONCLUSIONS

Results from the investigated cases showed the loss of either rig element leads to mast failure, but only one of the two correctly locates the failure point. Both cases exhibit two regions of high bending moments along the length of the mast, with the spreader case regions being located higher on the mast and of greater magnitude than

the D1 case. The deflected shapes of the mast are significantly different with regards to where curvature occurs. The time histories of the mast bending moments for the D1 case exhibits higher bending moments sooner, near the base of the mast and then later further up the mast. In contrast the spreader case exhibits higher bending moments at both locations simultaneously.

The time history of the rig tensions show a rapid drop in port side shroud tensions and increase in starboard tensions following both failures. This rapid change was then followed by a period of gradual change in the tensions with the starboard and some of the port side shrouds elements decreasing in tension as the rig deflections increased. Deflections in the spreaders were found to increase gradually with rig deflection.

The numerical approach to the post-failure structural investigation of the Groupama 4 mast breaking has been described. The investigation was able to distinguish between the failure modes of two closely located rig components. The use of an unsteady FSI approach meant that the aerodynamic loads on the rig could be accurately modelled as the flying shape changed. The FSI tool ARAVANTI has been shown to be capable of solving cases with highly transient, large deformation structural responses, while maintaining the stability of the FSI coupling. This capability can thus be applied to numerous other highly transient FSI problems such as sails undergoing wave-induced motions.

8 REFERENCES

1. AUGIER, B., BOT, P., HAUVILLE, F., and DURAND M., 'Experimental validation of unsteady models for fluid structure interaction', Application to yacht sails and rigs, *Journal of Wind Engineering and Industrial Aerodynamics 101*, 2012.

2. DURAND M., 'Interaction fluide-structure souple et légère, applications aux voiliers', *Ph.D. thesis, Ecole Centrale Nantes*, 2012.

3. REHBACH, C., 'Numerical calculation of three dimensional unsteady flows with vortex sheets', *16th Huntsville AIAA Paper 78-111*, 1978

4. CHARVET, T., HAUVILLE, F., HUBERSON, S., 'Numerical simulation of the flow around sails in real sailing conditions', *Journal of Wind Engineering and Industrial Aerodynamics 63*, 1996

5. HAUVILLE, F., DURAND, M., ROUX, Y., 'Modèle aèroélastique appliqué à la déformation d'un gréement', *European Journal of Environmental and Civil Engineering 12-5*, 2008

6. DURAND, M. HAUVILLE, P., BOT, P., AUGIER, B., ROUX, Y., LEROYER, A., VISONNEAU, M., 'Unsteady numerical simulation of downwind sails' *The Second International Conference on Innovation in High Performance sail Yachts*, 2010

9 AUTHORS' BIOGRAPHY

W. Menotti holds the current position of owner at Menotti Marine. He was responsible for the computations around the sail and rig. His previous experience includes sail design on various racing boats, ranging from small dinghies to super yachts.

M. Durand holds the current position of R&D director at K-Epsilon. He is responsible for FSI developments and sail simulations. His previous experience includes a PhD in fluid dynamics. He is also a world ranked match racing skipper (40th in world ranking for 2011).

D. Gross holds the current position of CFD engineer and naval architect at K-Epsilon. He has an MSc in marine CFD from the University of Southampton, where he specialized in multihull appendage FSI.

Y. Roux holds the current position of CEO of K-Epsilon, having, founded the company K-Epsilon in 2003. In partnership with laboratories, he and K-Epsilon develop numerical tools which are applied to unsteady aerodynamic, hydrodynamic and FSI studies.

D. Glehen holds the current position of GSEA DESIGN owner. He is responsible for the mast design and has worked with numerous French racing teams for the last 16 years. His previous experience includes IMOCA, VOR70, and MAXI multihull mast design. He was involved with Groupama Sailing Team for the last VOR70 campaign .

L. Dorez holds the current position of Head of Design at Groupama Sailing Team. In partnership with laboratories, structural design, hydrodynamic, and aerodynamic firms, he organizes the design and development of tools for Groupama Sailing Team.
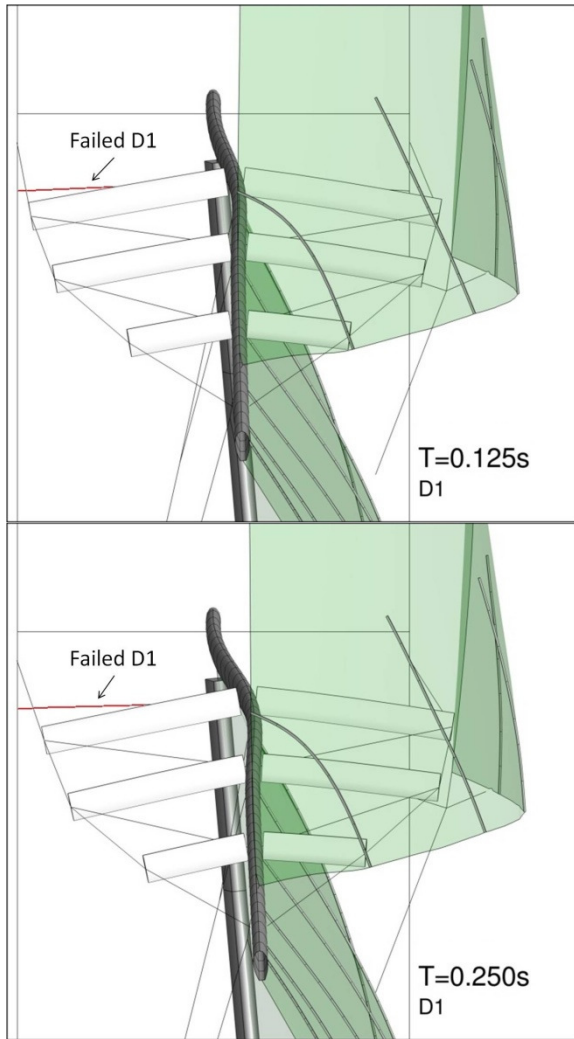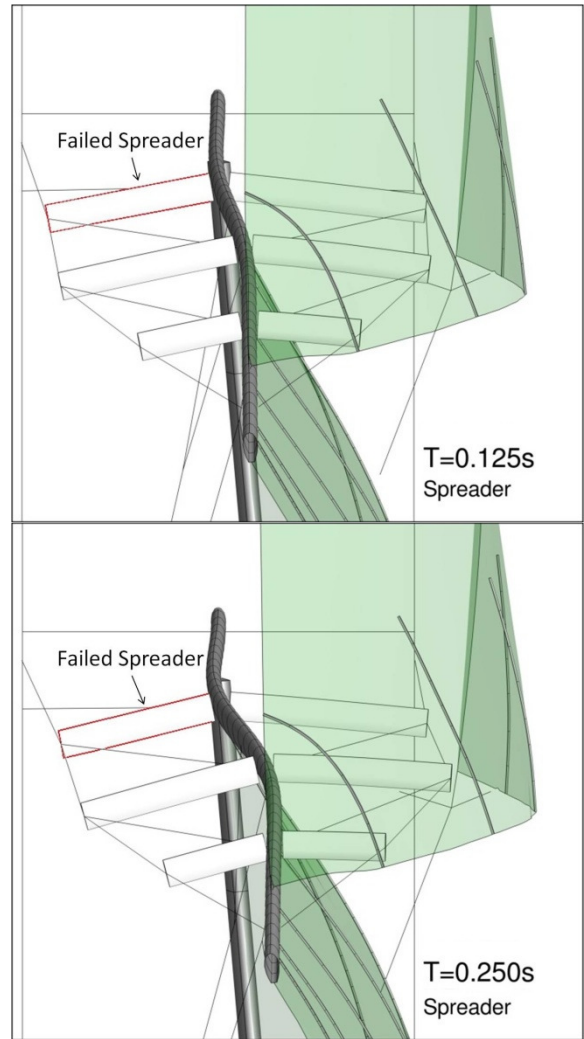
Figure 7: Time lapse of the mast failure, D1 case

Figure 8: Time lapse of the mast failure, Spreader case